

Water Resources Research

RESEARCH ARTICLE

10.1002/2015WR017751

Key Points:

- Laboratory evaluation of Oscillatory Hydraulic Tomography
- Provides robust estimates of aquifer hydraulic conductivity
- Multiple stimulation frequencies improve imaging results

Supporting Information:

- Supporting Information S1

Tanmoy Das

Correspondence to:
Y. Zhou,
zhou86@wisc.edu

Citation:

Zhou, Y.Q., D. Lim, F. Cupola, and M. Cardiff (2016), Aquifer imaging with pressure waves—Evaluation of low-impact characterization through sandbox experiments, *Water Resour. Res.*, 52, 2141–2156, doi:10.1002/2015WR017751.

Received 4 JUL 2015

Accepted 6 FEB 2016

Accepted article online 12 FEB 2016

Published online 24 MAR 2016

Tanmoy Das

1. Introduction

One of the greatest challenges in successfully managing groundwater contamination lies in the inherent difficulty of understanding heterogeneous subsurface properties. In groundwater contamination problems, in particular, characterization of the spatial variability of hydraulic conductivity is crucial for building accurate predictive transport models. The traditional approach for estimating aquifer properties including hydraulic conductivity (K) is through the analysis of individual pumping test results (i.e., drawdown curves) via analytical formulas that assume local aquifer homogeneity. The obtained conductivity value from such an analysis is an averaged or “effective” K of the aquifer over a large volume [Butler and Liu, 1993]. While analytically convenient, in realistic aquifers, this assumption of a homogenous subsurface is generally unrealistic, and the spatial variability of subsurface material must be understood through more careful analysis in order to accurately make solute and contamination transport predictions.

Numerous methods have been explored for estimating spatially variable hydraulic properties in the shallow subsurface. For example, small-scale stimulations such as partially penetrating slug tests or direct-push injection tests—which are less prone to averaging over large aquifer volumes—may be used to obtain local estimates of hydraulic parameters along a 1-D profile. These local parameter estimates may then be interpolated between sampling locations through geostatistical analysis—while incorporating geologic, hydrogeologic, and geophysical information—to create three-dimensional images of aquifer properties (e.g., as summarized in Koltermann and Gorelick [1996]). This characterization approach is conceptually simple and computationally efficient. However, exhaustive sampling at fine spatial densities may be necessary to obtain accurate interpolated maps of aquifer heterogeneity.

A recently developed approach to characterize subsurface properties is hydraulic tomography (HT), in which a series of constant-rate pumping tests are performed at different locations (“sources”), and pressure

change is monitored at several locations within the aquifer ("receivers"); the results of these tests are then jointly interpreted through tomographic analysis. Yeh and Liu [2000] originally performed a numerical hydraulic tomography study by applying a geostatistical inverse approach—the sequential successive linear estimator (SSLE)—to characterize 3-D spatial heterogeneity in a synthetic aquifer. They presented promising results, revealing detailed aquifer heterogeneity estimated from a series of five partially penetrating pumping tests, monitored at 20 observation locations in two boreholes.

Following these promising numerical results, several laboratory studies have been performed in order to evaluate the HT technology. In the first real-world experiment by Liu *et al.* [2002], two laboratory sandbox experiments were conducted and the SSLE was applied in order to characterize aquifer heterogeneity. In their analysis, steady state drawdowns due to pumping tests were used as the data for inversion, i.e., steady state hydraulic tomography. They demonstrated that hydraulic tomography reproduced major K heterogeneity patterns through comparison with the observable sandbox heterogeneity. Liu *et al.* [2007] then used sandbox experimentation to assess the effectiveness of transient hydraulic tomography—in which pressure data from several locations and monitoring times is analyzed—based on the SSLE algorithm developed by Vargas-Guzman and Yeh [2002]. Through transient hydraulic tomography, both hydraulic conductivity and storage coefficients were estimated. Inversion of five pumping tests produced maps of hydraulic conductivity variability consistent with the observed sandbox heterogeneity. Spatial variability in storage coefficients, in this case, was less detailed, and was thought to be primarily affected by packing within the sandbox. Later sandbox experiments have investigated hydraulic tomography in more complex aquifer scenarios, including DNAPL source zones [Illman *et al.*, 2010a] and unconfined aquifers [Zhao *et al.*, 2015]. Additionally, several analysis strategies have been applied to existing sandbox data, yielding information about the effectiveness of simplified numerical modeling strategies [Yin and Illman, 2009] and alternative inversion approaches [Liu and Kitanidis, 2011]. Finally, sandbox experiments have yielded important insights about practical issues that affect HT performance [Illman *et al.*, 2008], and about the degree of consistency between HT results and more traditional characterization results [Illman *et al.*, 2010b]. Overall, controlled  experiments have proven to be a valuable approach for evaluating the expected effectiveness of HT under real-world conditions.

04

Tanmoy Das

Recently, testing of HT has also been carried out in several field-scale experiments. Berg and Illman have investigated a highly heterogeneous glaciofluvial system using both transient HT [Berg and Illman, 2011] and steady state HT [Berg and Illman, 2013], and demonstrated that: (1) inverted conductivity maps are largely consistent with existing stratigraphic information; and (2) tomography improved the ability to predict aquifer response to independent pumping tests. In parallel, Cardiff *et al.* [2012, 2013] conducted 3-D  transient HT at a field research site and compared the obtained heterogeneity maps against profiles of K obtained from independent, detailed slug testing, finding a high correlation in the two sets of results.

05

Tanmoy Das

Hydraulic tomography, as applied in the above laboratory and field studies, uses standard constant-rate pumping tests and thus relies on extensive extraction or injection of water at pumping locations, which could potentially cause spreading of subsurface contaminants if applied at a contaminated site, and/or could incur significant treatment costs for handling extracted waste water. Traditional pumping tests can also require significant field time before steady state conditions are achieved, meaning that either: (1) long-term field effort is needed to obtain steady state HT data or (2) more cumbersome transient numerical modeling is required to analyze nonsteady hydraulic tomography data. In the hydrology literature, a few other tomography approaches have been suggested which avoid mass water extraction. Vasco *et al.* [2000] and Brauchler *et al.* [2003, 2007] collected data from impulse responses (i.e., slug interference tests) and inverted the pressure wave's travel time and amplitude to characterize subsurface properties. Their analysis, however, requires aquifer flow to be simulated using a physically approximate "zeroth-order" model, and the range of feasible testing distances is limited by the propagation of the small-amplitude slug testing signals.

06

Tanmoy Das

While slug tests and pumping tests represent well-known methods for aquifer testing, some studies have investigated oscillatory pumping approaches, in which water is extracted and reinjected periodically. This approach was first theoretically analyzed in the area of petroleum reservoir testing [Kuo, 1972]. Though they require more specialized equipment to implement, the practical advantages of oscillatory pumping tests are many, including: (1) no net injection or extraction of water, (2) little movement of existing contaminants due to minimal disruption of ambient hydraulic gradients, (3) minimal impact of model boundary conditions, and (4) the ease of extracting resulting oscillatory signals from noisy data. Soon after its  introduction, oscillatory pumping tests were applied to aquifer imaging [Vasallo *et al.*, 1998].

07

Tanmoy Das

discussion in the petroleum literature, Black and Kipp [1981] developed analytical solutions to study pressure responses generated by oscillatory pumping tests. Still, these pumping tests have been applied only occasionally in field studies—Bernabe *et al.* [2005], Rasmussen *et al.* [2003], Renner and Messar [2006], Main-eult *et al.* [2008], Becker and Guiltinan [2010], Guiltinan and Becker [2015], and Rabinovich *et al.* [2015] represent the few examples in which oscillatory or periodic testing was used to estimate subsurface properties. Each of these analyses, however, assumed a homogeneous aquifer and fit oscillatory data to a homogeneous model. Lavenue and de Marsily [2001], however, performed a field application of periodic pumping tests in which the pilot point inverse method was used to invert the resulting data and estimate heterogeneous parameters. As far as we are aware, their study is the only prior published work in which periodic pumping test data have been used to infer heterogeneous aquifer parameters.

Combining the concepts of oscillatory pumping tests with hydraulic tomography, Cardiff *et al.* [2013] presented the mathematical theory for a new aquifer characterization approach, Oscillatory Hydraulic Tomography (OHT). In this strategy, several periodic pumping tests of different frequencies are used for aquifer stimulation, and responses are analyzed tomographically using a fast, steady-periodic groundwater flow model. Numerical results in this work demonstrated that different frequencies of testing provide additional information about aquifer heterogeneity. Much like in seismological investigations, OHT data from high-frequency pumping tests tend to be more sensitive to subsurface properties in the “near field,” whereas low-frequency pumping tests are sensitive to a broader region, but appear to have less resolution.

To assess the accuracy of the assumed physics governing oscillatory pressure wave propagation, and to evaluate the practical effectiveness of OHT, we have built a laboratory sandbox and use laboratory data collected from sandbox OHT experimentation to evaluate the real-world performance of this new technology. The focus of the research presented here is to provide an experimental confirmation of the theory of OHT for testing frequencies that are reasonable in practical hydraulic application (generally < 1 Hz). The instrumented laboratory sandbox is filled with a visible distribution of different porous media materials (sands and gravels), and aquifer pressure responses are recorded during oscillatory pumping tests at a variety of frequencies. Through these tests, we provide the first experimental use of the steady-periodic physical model developed for studying oscillatory flow, and we likewise assess the real-world capability of OHT for characterizing aquifer heterogeneity.

The remainder of this work is organized as follows: We first describe the design and instrumentation of the sandbox in section 2. The stimulations performed—which consisted of oscillatory pumping tests performed at multiple frequencies and locations—are described in section 3. In section 4, we discuss data processing of OHT data, in which pressure signal properties are extracted from raw pressure time series data. In section 5, we discuss the tomography approach used, including: (1) the forward model, consisting of a groundwater flow model in the (steady-periodic) phasor domain; (2) the applied geostatistical inversion approach; and (3) methodologies for estimating and propagating data errors and uncertainties. Finally, we present and discuss the results of OHT imaging in section 6, and offer guidance for field applications based on the lessons learned.

2. Experimental Setup

The sandbox used in our experimentation is designed to evaluate aquifer properties within an effectively two-dimensional domain, packed with materials of known hydraulic properties. It is also built to be compatible with organic solvents such as DNAPLs to allow contaminant transport testing. The total sandbox size is 1.78 m wide, 0.77 m tall, and 0.14 m thick (Figure 1) with an internal volume of 1.5 m \times 0.75 m \times 0.1 m. The limited thickness dimension enables the sandbox, when properly packed, to realistically represent two-dimensional flow. The sandbox is constructed of 2 cm thick Plexiglas (Midland Plastics), bonded by a mixture of Plexiglas and chloroform. The front side of the sandbox contains ports for observing pressure changes at 25 equally spaced locations (Figure 1). Fiber-optic pressure transducers were installed in the ports to record pressure changes due to oscillatory pumping at different frequencies. To maintain compression and vertical stability of the sandbox, we clamped Unistrut metal support beams at the front and back of the sandbox.

The sandbox built for current research is also designed to simulate natural fluid flow and solute transport in a confined or unconfined aquifer under a controlled environment. The sandbox contains water reservoirs,

08

Tanmoy Das

09

Tanmoy Das

10

Tanmoy Das

11

Tanmoy Das

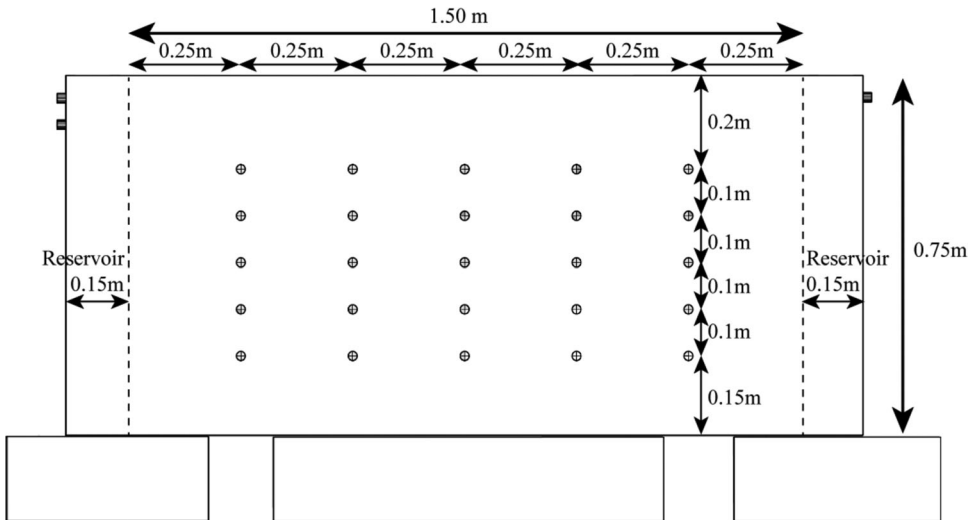


Figure 1. Diagram of sandbox construction, showing arrangement of ports, with internal volume of $1.5 \text{ m} \times 0.75 \text{ m} \times 0.1 \text{ m}$. Outlets on far left and far right allow adjustment of reservoir static water levels. Metal supports at bottom raise sandbox above ground and provide stability.

maintained at a constant water level, on the left and right ends of the domain. A fine mesh barrier, 400 mesh ($37 \mu\text{m}$), capable of filtering sands while allowing flow of water, is attached to the Plexiglas that separates the water supply reservoirs from the porous media domain. The constant head boundaries are maintained by constant water supply at one end of the flow cell and overflow at the other end. Toward the top of the reservoirs, copper hose connectors are installed to allow the flow system to maintain at a controlled water level. At the bottom of one reservoir, a third copper hose connector is installed to allow water drainage of the sandbox when not in use. The base (bottom) of the sandbox is solid Plexiglas, representing a no-flow boundary. Finally, for the experiments performed in this work, the top of the sandbox was sealed with low-permeability bentonite clay, which is approximated during modeling as a no-flow boundary as well. Five locations in the sandbox are setup for pumping, with a 25.4 mm diameter air stone diffuser installed. The air stone diffuser acts as a stable porous media that distributes injected water throughout the thickness while also preventing sand invasion into the pump.

Fiber-optic pressure transducers (Model FOP-MIV-NS-779A, FISO Technologies, Quebec, Canada) with a sampling frequency of 125 Hz are used to detect pressure variations at the observation locations. All pressure transducers are connected to a central data acquisition system, which records relative pressure changes throughout the duration of the experiment. The high-accuracy, custom-built fiber-optic transducers used have a resolution of $<0.001 \text{ psi}$. We converted psi to corresponding head in meters, assuming a density of 1000 kg/m^3 , resulting in a head resolution of $<1 \text{ mm}$. Exact accuracy specifications for these custom-built sensors are not published by FISO. However, in preliminary calibration experiments, sensors accurately detected pressure changes of 1–2 mm of head.

During each experiment, the sandbox was packed with sedimentary material (Figure 2a) and then saturated with fresh tap water at room temperature. While minor variations in density or viscosity of the fluid are possible due to temperature and total dissolved variations, the uncertainty introduced is considered to be minor relative to other typical sources of experimental uncertainty, such as atmospheric pressure variations, absolute sensor placement locations, sensor resolution, pumping rate errors, and the like.

The sandbox and monitoring equipment can be used to perform a variety of hydraulic tests. In particular, the majority of testing analyzed in this work consisted of oscillatory pumping tests. To perform oscillatory pumping tests, we utilized a custom-built hydraulic piston controlled by an electric motor with attached flywheel (Figure 2b). By attaching the piston to a particular location on the flywheel and setting the electric motor speed, we control the total cycle volume and the period, respectively, of the test. This apparatus was attached to the sandbox at pumping ports to perform the oscillatory pumping tests described in section 3.

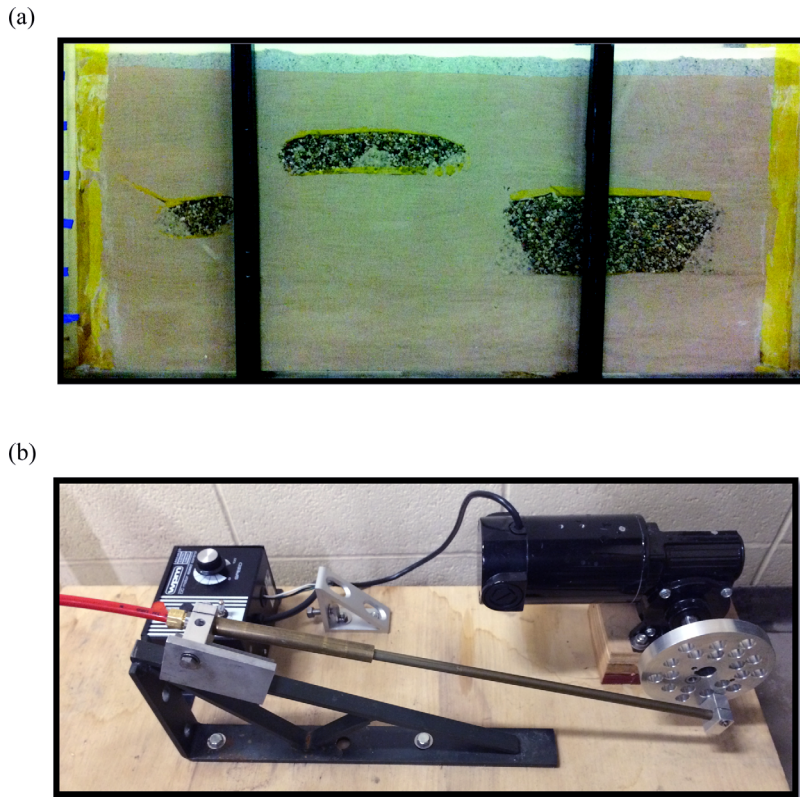


Figure 2. Experimental apparatus: (a) heterogeneous sandbox packing, front view. Background material is sand, with heterogeneities of gravel. (b) Design of oscillating signal generator. Area of piston is 0.785 cm^2 . Stroke length is adjusted using flywheel holes, to control desired pumping volumes. Here piston volume is set to 4 mL.

However, this apparatus can be detached in order to perform standard constant-rate pumping via peristaltic pumps.

The described laboratory sandbox setup allows controlled testing including constant-rate pumping tests, cross-hole pumping tests, and also oscillatory pumping tests under confined or unconfined conditions. It can further be used to test periodic signal propagation during transport of contaminants such as high-viscosity DNAPLs in different types of porous media. The data acquisition system is capable of monitoring the pumping location driving pressures and monitoring location pressure responses at the same time.

3. Oscillatory Flow Testing

To investigate the response of aquifers to periodic forcing across a range of frequencies, we performed oscillatory pumping tests on two experimental setups. The first experimental setup represented a homogeneous aquifer, in which the sandbox was filled with homogeneous commercial silica sand with a hydraulic conductivity estimated at $1.1 \text{E-}4 \text{ m/s}$ ($\ln(K) = -9.1$), as determined from falling-head permeameter testing. The second experimental setup represented a heterogeneous aquifer (Figure 2) with higher K ($2.7 \text{E-}3 \text{ m/s}$, $\ln(K) = -5.9$) gravel patches distributed within the lower K background sand. In this case, we created roughly rectangular gravel features embedded in the background sand, with dimensions ranging from large ($\sim 50 \text{ cm} \times 20 \text{ cm}$) to small ($\sim 20 \text{ cm} \times 10 \text{ cm}$) to represent a simple heterogeneous aquifer, and to test the ability of our tomography to resolve heterogeneities of different scales. A series of oscillatory pumping tests were performed at pumping ports at nominal periods of 2, 5, 10, and 20 s. During each test, oscillatory pumping is continued until steady-periodic conditions—represented by consistent signal amplitude and phase—are observed at all data collection locations. The pumping location was then varied throughout the domain while observation locations remain the same (Figure 3).

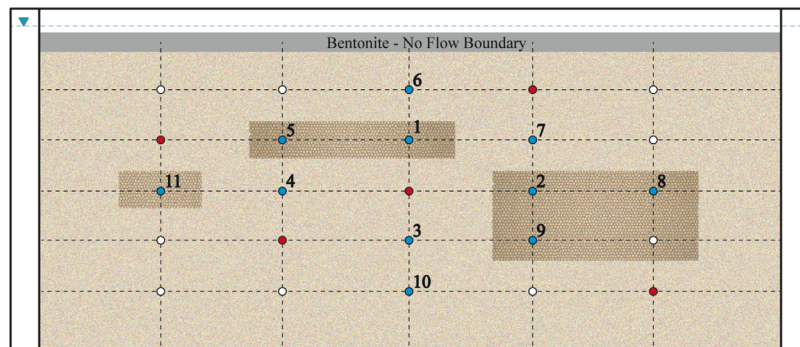


Figure 3. Experimental design. Pumping locations indicated in red; observation locations indicated in blue; white ports not used in this work. Center red source point is defined as row 3, column 3. Dark brown color patterns represent gravel heterogeneity placements relative to sensor locations.

One concern in performing quickly varying pumping tests is the possibility of introducing non-Darcian responses. However, this concern can be mitigated by using small total pumping volumes, which results in small volume flow rates. During the experimental data collection, we tested several combinations of total volume (piston stroke length) and periods to ensure linear (Darcian) response, eventually settling on a total cycling volume of 4 mL. We discarded non-Darcian flow tests in which the relationship between flow rate and head change amplitude was nonlinear. Each data collection starts with zero pressure change, and generally after 5–6 periodic cycles (see Figure 4), it transitions to steady-periodic status, in which the amplitude and phase of all signals are visually observed to be consistent. Oscillatory pumping tests were performed on both the homogeneous and heterogeneous sandbox using the same set of pumping volumes, pumping locations, and observation locations.

12

Tanmoy Das

13

Tanmoy Das

4. Data Processing

During each oscillatory pumping test, a sinusoidal pressure wave of a given period, i.e., either 2, 5, 10, or 20 s is produced throughout the sandbox, and these pressure changes are recorded at an array of observation locations. The collected time series data are periodic with a clearly visible signal (e.g., Figure 4) and overall high signal-to-noise ratio (SNR). To process the data for inversion, spectral analysis is performed on

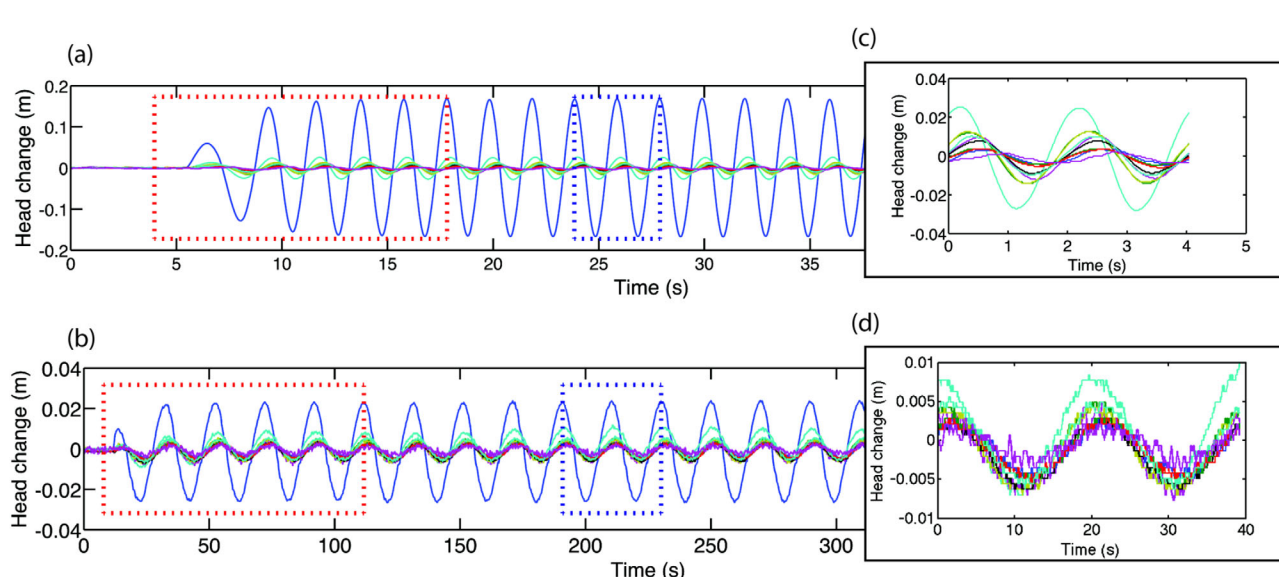


Figure 4. Pressure responses measured during oscillatory testing with nominal (a) 2 s and (b) 20 s period. Red dashed box shows transition from pretesting period to steady-periodic response with a consistent amplitude and phase. (c and d) Magnified views of steady-periodic pressure responses (blue dashed box) at observation locations. Data in figures above are from heterogeneous aquifer testing.

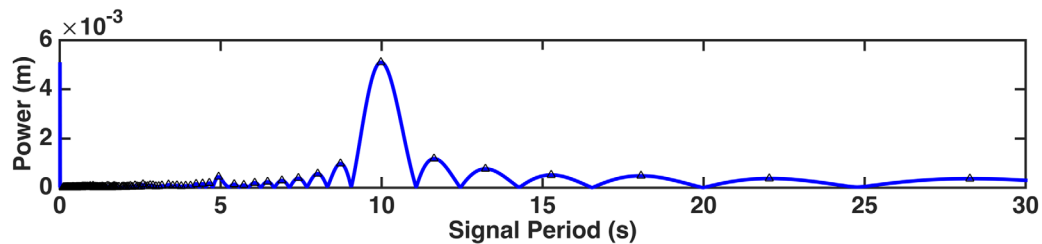


Figure 5. Sample period spectrum plot for one set of analyzed 10 s period oscillatory data.

the pressure change time series collected at each observation location to extract the signal amplitudes and phases associated with the given pumping frequency. The Fast Fourier Transform (FFT) algorithm is used to analyze the time series data to obtain Fourier coefficients, which store information about the oscillation frequencies as well as their amplitude and phase shift.

In our testing, each oscillatory pumping test produced 12 data sets, with one data set representing the pumping port pressure, and the rest of the data sets representing receiver responses. Figure 5 shows one example of a data set collected during oscillating pumping at a nominal 10 s period, and the corresponding frequency domain power. In the frequency spectrum plot, the highly dominant frequency component is about 0.1 Hz (10 s period). While we show only one example, almost all of the data sets recorded (including those at the pumping location) contain a single dominant frequency component, and in all cases, we found that the sandbox response appeared to be highly linear, i.e., the observation location signals have the same dominant frequency component as the pumping location. In order to apply the steady-periodic numerical model (discussed in the following section), each observation is represented by the Fourier coefficients measured at the corresponding point in the sandbox, which describes the amplitude and phase of the steady-periodic signal. To ensure that the dominant signal components are represented by the obtained Fourier coefficients, we can convert the coefficients back to the time domain and fit to the observed data (Figure 6). In all cases analyzed, the standard deviation between these fit curves and the raw observed data is on the order of 10^{-3} – 10^{-4} m. The result provides confidence that the dominant frequency in FFT captures the majority of the response observed in the transient pressure signals.

Before attempting tomography of the collected data, the signal characteristics were first visualized to perform quality control and assess any data processing issues. An example, shown in Figure 7, displays the amplitudes and phases of collected data during comparable tests in the homogeneous and heterogeneous setups, with amplitude normalized by the amplitude at the pumping location, and the phase represented by the difference from the phase at the pump (Figure 7). These plots provide a fast visual method for inspecting oscillatory testing data, which may also be useful in field investigations. General trends observed through these analyses were consistent with expectations, as follows: (1) the amplitude of the head response at each location is dependent on its distance to the pumping port. Observation locations that are closer to the pumping port achieve larger amplitudes in head change and vice versa. Similarly, phase delay also increases with distance from the pumping port in all cases; (2) the normalized amplitude attenuation with distance is less prominent in lower frequency than in higher-frequency oscillatory pumping tests; (3) in

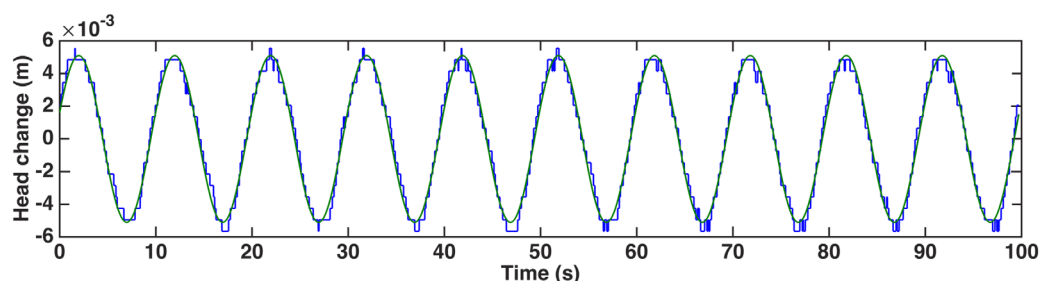


Figure 6. Comparison between observed data (blue) and representation using a single-component sinusoid (green).

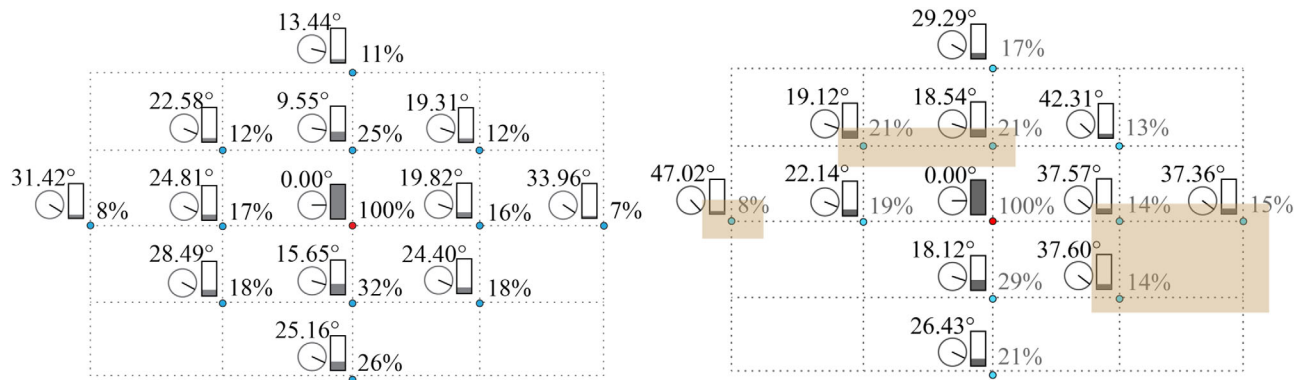


Figure 7. Phase and amplitude summary from testing with nominal 20 s period for (left) homogeneous and (right) heterogeneous aquifer. Clock indicator represents phase change and bar represents amplitude change, both relative to source. Shaded areas on heterogeneous aquifer represent location of gravel in background sand.

the homogeneous aquifer, the amplitude and phase lag appear to be dependent primarily on distance from the pumping location, whereas in the heterogeneous case, the phase lag and amplitude are both affected by local heterogeneity, and thus are not as radially symmetric as the homogeneous responses (Figure 7, right).

One key benefit of using oscillatory signals with a known frequency for aquifer stimulation is that the signal is easily extractable from observed data in the presence of significant noise and even sensor drift. Additionally, error in signal Fourier coefficients (or similarly, amplitude and phase estimates) can be reduced through increased signal lengths of time series measurements. In field investigations, this trade-off between investigation time and signal robustness may prove highly beneficial. Through preliminary analyses, we discovered that Fourier coefficients could be accurately estimated with as little as two periods-worth of data, presumably due to the high sampling frequency and high SNR of our laboratory data. Analysis of longer time series records did not produce significantly different Fourier coefficient estimates. For all inversions presented in the following sections (sections 6.1–6.3), we used 10 periods of time series data to determine the Fourier coefficients.

5. Imaging Approach

5.1. Physical Model

The phasor-based (steady-periodic) groundwater flow model can be used to describe propagation of oscillations at a given frequency. A detailed description of the phasor model derivation can be found in *Cardiff et al* [2013]. By replacing hydraulic head with $\Phi_\omega(\mathbf{x})$ [L], the wave phasor (a complex-valued field variable), the standard groundwater flow model can be expressed as follows:

$$i\omega S_s \Phi_\omega = \nabla \cdot (K \nabla \Phi_\omega) + Q, \quad \forall \mathbf{x} \in \Omega \quad (1)$$

$$\Phi_\omega = 0, \quad \forall \mathbf{x} \in \Gamma_d \quad (2)$$

$$\nabla \Phi_\omega \cdot \mathbf{n} = 0, \quad \forall \mathbf{x} \in \Gamma_n \quad (3)$$

where Ω is the domain of interest; \mathbf{x} is a vector of spatial coordinates [L]; Γ_d and Γ_n represent Dirichlet and Neumann boundaries, respectively; $Q(\mathbf{x})$ is a scalar field giving peak volume flow rates [$1/T$]; ω is the angular frequency of the oscillation [radians/ T]; $S_s(\mathbf{x})$ is a scalar field of specific storage values [$1/L$]; and $K(\mathbf{x})$ is a scalar field of hydraulic conductivity values [L/T] (assumed isotropic). This model, which contains no temporal derivatives, can solve for the steady-periodic response within the aquifer, after initial transient response has dissipated. The phasor field solved for in the numerical model is then equivalent to the Fourier coefficients of time series data that would be measured at any point in space. Thus, measured responses from lab or field tests (Fourier coefficients extracted from steady-periodic hydraulic heads) can be inverted using this fast-running model of aquifer response. For use within the inversion framework, the model is numerically simulated in a heterogeneous domain using a finite volume-based discretization of the phasor equations presented above, as developed in MATLAB. The sandbox model in our case was discretized into 1800

cells with each cell of dimensions $0.025 \text{ m} \times 0.025 \text{ m} \times 0.1 \text{ m}$. Individual forward model runs, using this discretization, require roughly 0.2 s.

5.2. Inverse Model

OHT data can be inverted using any standard method for ill-posed (tomographic) inverse problems. In this work, we utilize the quasi-linear geostatistical theory developed by *Kitanidis* [1995]. We utilize this algorithm to estimate the spatial distribution of both K and S_s in the laboratory sandbox aquifer, by inverting the Fourier Coefficients of the observed pressure response (as discussed in detail in *Cardiff et al.* [2013]). To obtain K and S_s tomograms from multiple oscillatory pumping tests, we solve an inverse problem for oscillatory flow conditions. Input data to the inverse model include measured sinusoidal and cosinusoidal coefficients (i.e., the real and imaginary parts of the Fourier coefficients) at each stimulation frequency along with the covariance matrix of the errors of these coefficients and an a priori estimate of expected heterogeneity statistics. We note, at this point, that another approach to inversion of steady-periodic data is inversion of amplitude and phase of the signal, which contains exactly the same information as the Fourier coefficients. While perhaps more intuitive to interpret, phases are nonlinear functions of the observed Fourier coefficients, and thus their use can introduce additional nonlinearity into the inverse problem (especially near the branch cut where phases approach 2π).

The objective function optimized is:

$$\min_{\mathbf{s}, \boldsymbol{\beta}} \frac{1}{2} (\mathbf{y} - \mathbf{h}(\mathbf{s}))^T \mathbf{R}^{-1} (\mathbf{y} - \mathbf{h}(\mathbf{s})) + \frac{1}{2} (\mathbf{s} - \mathbf{X}\boldsymbol{\beta})^T \mathbf{Q}^{-1} (\mathbf{s} - \mathbf{X}\boldsymbol{\beta}) \quad (4)$$

where, given m measurements and n parameters, \mathbf{s} is the $(n \times 1)$ vector of parameter values (K and S_s in each grid cell); \mathbf{y} is the $(m \times 1)$ vector of data (real and imaginary parts of the Fourier coefficients measured at each location and each frequency); $\mathbf{h}()$ is the physical forward model described above, \mathbf{R} is the $(m \times m)$ covariance matrix of data errors (derived from the covariance matrix of Fourier coefficient errors from the normal equations [see e.g., *Bakhos et al.*, 2014]), \mathbf{X} is a $(m \times p)$ vector of drift function values, $\boldsymbol{\beta}$ is a $(p \times 1)$ vector of drift coefficients, and \mathbf{Q} is the $(n \times n)$ prior expected parameter covariance. \mathbf{Q} is computed based on the expected variance of the K and S_s fields ($\sigma_{lnK}^2 = 1.17$, $\sigma_{lnS_s}^2 = 0.2$) and assumed correlation scales ($\lambda_x = 0.6 \text{ m}$, $\lambda_y = 0.2 \text{ m}$). In this example, as in *Cardiff et al.* [2013], we assumed the sandbox heterogeneity can be modeled as a stationary, constant-mean random field. While this approach necessarily represents an assumption (which may be violated in reality) about the statistical structure of sandbox heterogeneity, previous work [*Cardiff and Barrash*, 2011; *Illman et al.*, 2015] has demonstrated that the geostatistical assumption yields robust estimations in ill-posed inverse problems, i.e., it allows the inversion results to largely be driven by the data alone. To focus on the data content in oscillatory data and limit the impact of incorrect inversion choices, the variance and correlation length of K and S_s (variogram) were computed based on the permeameter tested parameter and our knowledge of the sizes of heterogeneous structures in the sandbox. Such information will generally not be available during processing of real-world field data. However, prior work has demonstrated that these parameters have limited impact on inversion results, unless correlation scales or variances are grossly overestimated or underestimated [*Yeh and Liu*, 2000]. Likewise, statistical approaches such as restricted maximum likelihood [*Kitanidis*, 1995] can be applied when parameter field variances and correlation lengths are highly uncertain. All inverse modeling runs presented here were executed using a MacBook Pro with 2.6 GHz Intel Core i7 processor and 16 Gb of RAM. Individual inversion run-times increase with increasing amount of data input. However, the total inversion run time is less than 10 min for any individual imaging result presented herein.

5.3. Error Propagation

Transient data, in practice, are contaminated with noise, which results in errors in the Fourier coefficients obtained via signal processing. *Bakhos et al.* [2014] used linear regression to recover signals from a set of noisy time series measurements. In specific, they looked into the effectiveness of linear regression on four common types of noise observed in practice: white noise, white noise with a jump in the signal, white noise with a linear drift, and correlated noise. Error in estimates of Fourier coefficients is quantified by a data covariance matrix assuming time series data noise (ε) is Gaussian, $\varepsilon \sim \mathcal{N}(0, \sigma^2)$. For instance, time series hydraulic head data can be expressed as:

$$\mathbf{d} = A_\omega \cos(\omega \mathbf{t}) + B_\omega \sin(\omega \mathbf{t}) + \boldsymbol{\varepsilon} \quad (5)$$

where \mathbf{d} represents the data vector at a particular measurement location and frequency; \mathbf{t} is the vector of measurement times; $\cos()$ and $\sin()$ are defined as being performed element-wise on a vector; and A_ω and B_ω represent the cosinusoidal and sinusoidal coefficients, respectively, to be estimated. If the time interval between data measurement Δt is small and total sampling time T_s is a multiple of the signal period, the covariance matrix of Fourier coefficient errors (\mathbf{R}) can be expressed as [Bakhos *et al.*, 2014]:

$$\text{Cov} \left(\begin{bmatrix} A_\omega \\ B_\omega \end{bmatrix} \right) = \mathbf{R} \approx 2\sigma^2 \frac{\Delta t}{T_s} \begin{pmatrix} 1 & 0 \\ 0 & 1 \end{pmatrix} \quad (6)$$

Here data noise—representing both sensor noise and overall epistemic errors in the model—is assumed to have a standard deviation (σ) of $\sim 2\text{mm}$, and sampling at 125 Hz gives a time interval between measurements (Δt) of 0.008 s. In initial tests of inversion, we utilized the actual sampling time T_s for each analyzed time series. However, poor convergence (in terms of obtaining adequate data fit) was observed during these initial tests. Instead, we utilized a consistent assumed sampling time of 20 s across all data, which produced better convergence results. A larger sampling time gives a smaller data error covariance matrix, and therefore gives more weight to the data fitting in the optimization step during inversion (see equation (4)). On the other hand, a 20 s sampling time is appropriate to obtain at least one complete period of data across all pumping periods, and is therefore reasonable for the periods being tested. The data covariance matrix assumed across all inversion cases presented below is thus a scaled identity matrix with diagonal elements equal to $4 \times 10^{-9} \text{ m}^2$. Since the theoretically developed data weights suggested earlier appeared to give poor results during inversion of actual (nonsynthetic) data, further research is necessary as to what physical or numerical processes are affecting the inversion results. We comment further on this issue in section 7.

6. Results and Discussion

In this section, we analyze OHT imaging as applied to the laboratory sandbox, and investigate the influence of different factors on the obtained tomograms. The best K tomograms, which will be used for comparison, are assumed to be obtained when using all frequencies of data (2, 5, 10, and 20 s) from all pumping tests. For simplification, we will call pumping locations “sources” and observation locations “receivers” in the following discussion. In section 6.1, we discuss the impact of multifrequency data on K tomograms by comparing single frequency and multifrequency inversion results. In section 6.2, we discuss the improvement in the K tomogram using multisource tomography compared to single-source tomography. In section 6.3, we analyze the influence of receiver locations and receiver density on the K tomogram. Finally, in section 6.4, we quantitatively assess different tomograms obtained from different analysis cases.

We note that in each inversion, we estimated both spatially distributed K and S_s in all grid blocks of the numerical model and allow both K and S_s to vary as a function of space. As has been discussed previously, imaging results for hydraulic conductivity are affected not only by inherent ill posedness in the inverse problem, but also by “aliasing” that can occur between K variability and S_s variability. Li *et al.* [2005] investigated this issue, and showed through synthetic experiments that the effect of aliasing (via an aliasing ratio) for hydraulic conductivity is only 5% even in the case where S_s variance is comparable to K variance. In a separate synthetic investigation with less drastic storage coefficient variance, Cardiff and Barrash [2011] further showed that assuming spatially constant values for storage coefficients has a very minor impact on the estimation of conductivity, implying minimal impact from aliasing. In supporting information associated with this work (online), we present both K and S_s fields estimated in each inversion case, allowing further investigation of this issue.

The tomograms obtained when using all data for both the heterogeneous and homogeneous sandbox are shown in Figure 8. We note that in the homogeneous case (Figure 8a), some heterogeneity is still visible in the obtained tomogram, though the overall range of variability is relatively low (estimated $\ln(K)$ standard deviation = 1.17). In this case, these heterogeneities are likely artifacts of the inversion, perhaps caused by microscale heterogeneities that impact high-frequency and low-frequency tests in different ways—and perhaps also suggesting that imaging of small K contrasts will be difficult. However, in the heterogeneous K sandbox tomogram, the positions of the larger high- K gravel deposits are clearly visible. Based only on the

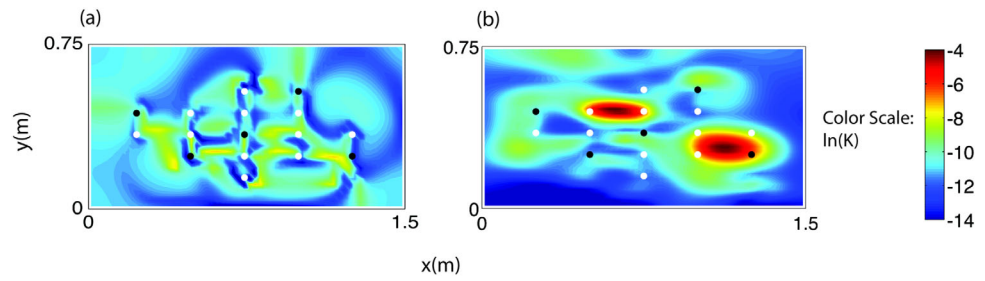


Figure 8. Best K tomogram, inverted when using all frequencies and all pumping tests, for both (a) homogeneous and (b) heterogeneous aquifer.

obtained data from the heterogeneous sandbox, Figure 8b thus represents our “best estimate” of the true material properties in the heterogeneous sandbox, and will be used as the basis for comparison with other inversions of the heterogeneous sandbox data.

6.1. Signal Frequency Influence on K Tomogram

One key aspect of OHT—which has been shown theoretically—is that different frequencies of aquifer stimulation provide different sensitivities to heterogeneity within a volume. Thus, a single pumping location can be used to obtain different sets of information about aquifer heterogeneity by altering the pumping frequency. To demonstrate this impact, in our analysis, we provide results of inversion in which a single pumping location is utilized, but progressively larger numbers of testing frequencies are inverted. Our results show two single frequency inversions (2 and 20 s), a joint inversion of 2 and 20 s oscillations, and a joint inversion of 2, 5, 10, and 20 s oscillations (Figure 9). These experimental results agree qualitatively with numerical simulations presented in *Cardiff et al. [2013]*, i.e., the high-frequency oscillations are more sensitive to “near-field” parameters and low-frequency oscillations produce more diffusive sensitivities throughout aquifer. The results also qualitatively demonstrate that progressive improvement in aquifer imaging results are obtained by jointly inverting multiple frequencies’ response.

6.2. Source Location Influence on K Tomogram

To obtain truly tomographic results, we implemented multiple source and receiver combinations using 2 s frequency data. In Figure 10, the receiver locations remain the same while source locations (i.e., additional pumping tests) are gradually added. By adding more source locations, we are qualitatively able to obtain improved resolution of both fine-scale and large-scale aquifer features in the K tomogram. When using two sources for imaging, we can already obtain a K tomogram that well represents the visible sandbox pattern.

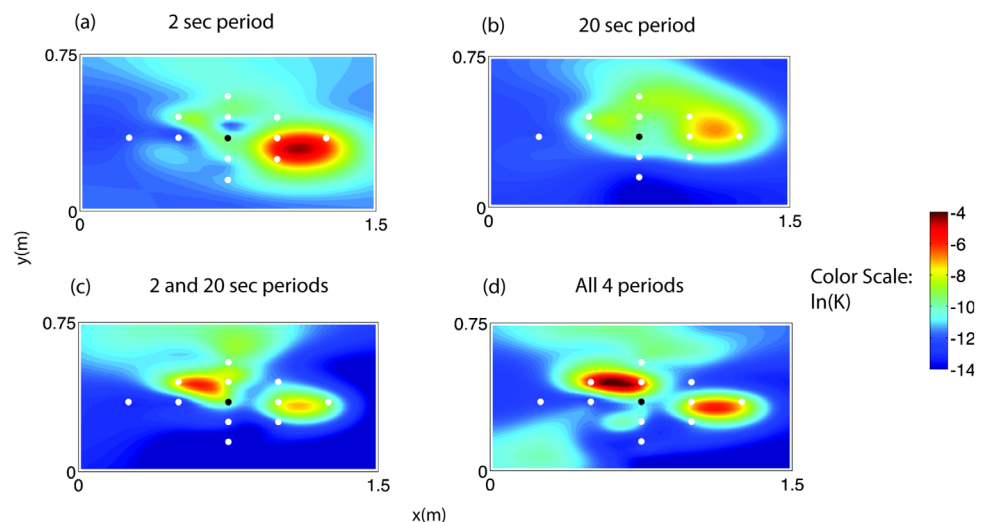


Figure 9. Comparison of inversion results using a single pumping location (center: row 3, column 3, as indicated by black point), as number of testing frequencies is increased. White points show observation locations used.

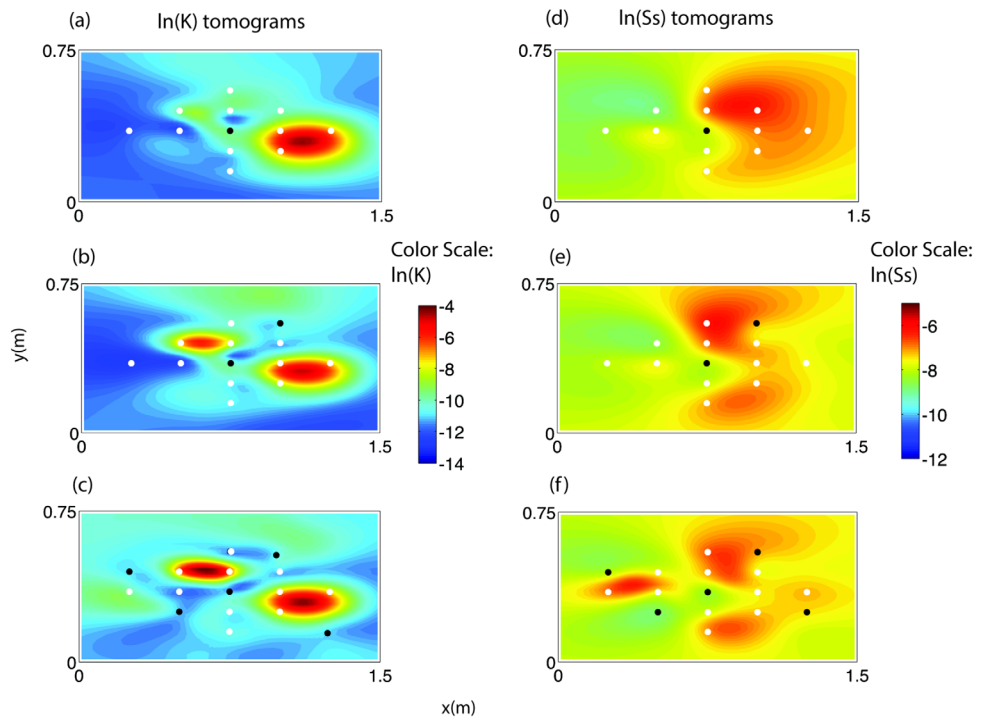


Figure 10. Improvements in K and S_s tomograms as more pumping tests are included in inversion of single-frequency (2 s) data. Black points represent pumping locations inverted; white points are observation locations.

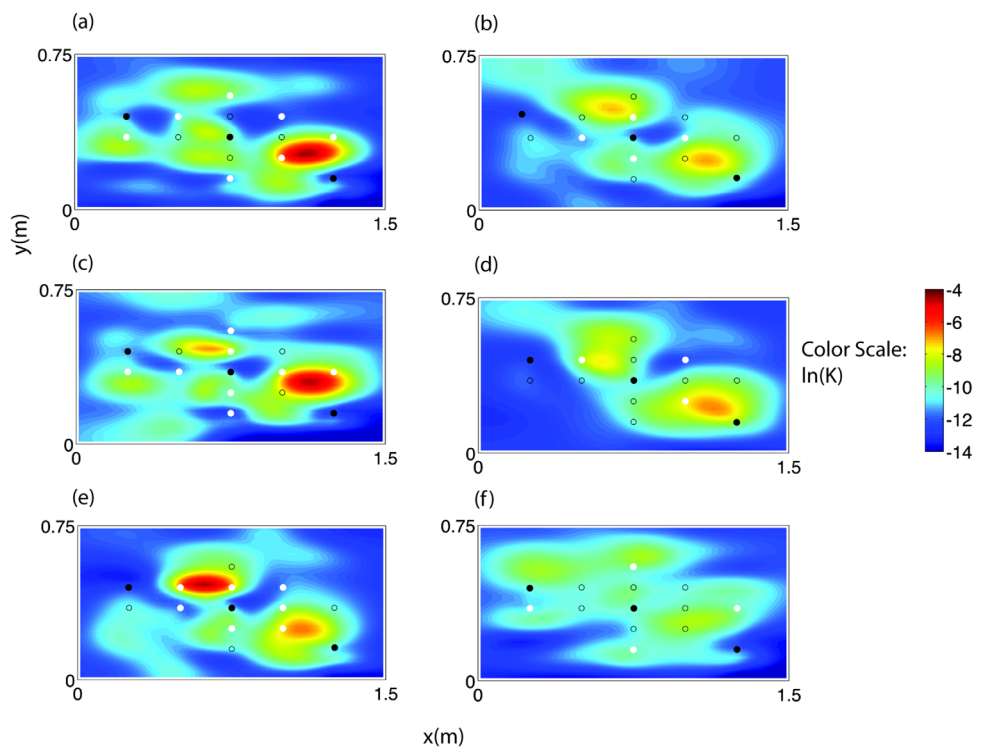


Figure 11. K tomograms, testing influence of receiver distribution on inversion. Black solid points represent source location, white solid points represent receiver location, and black empty points represent inactive receiver locations (data not used).

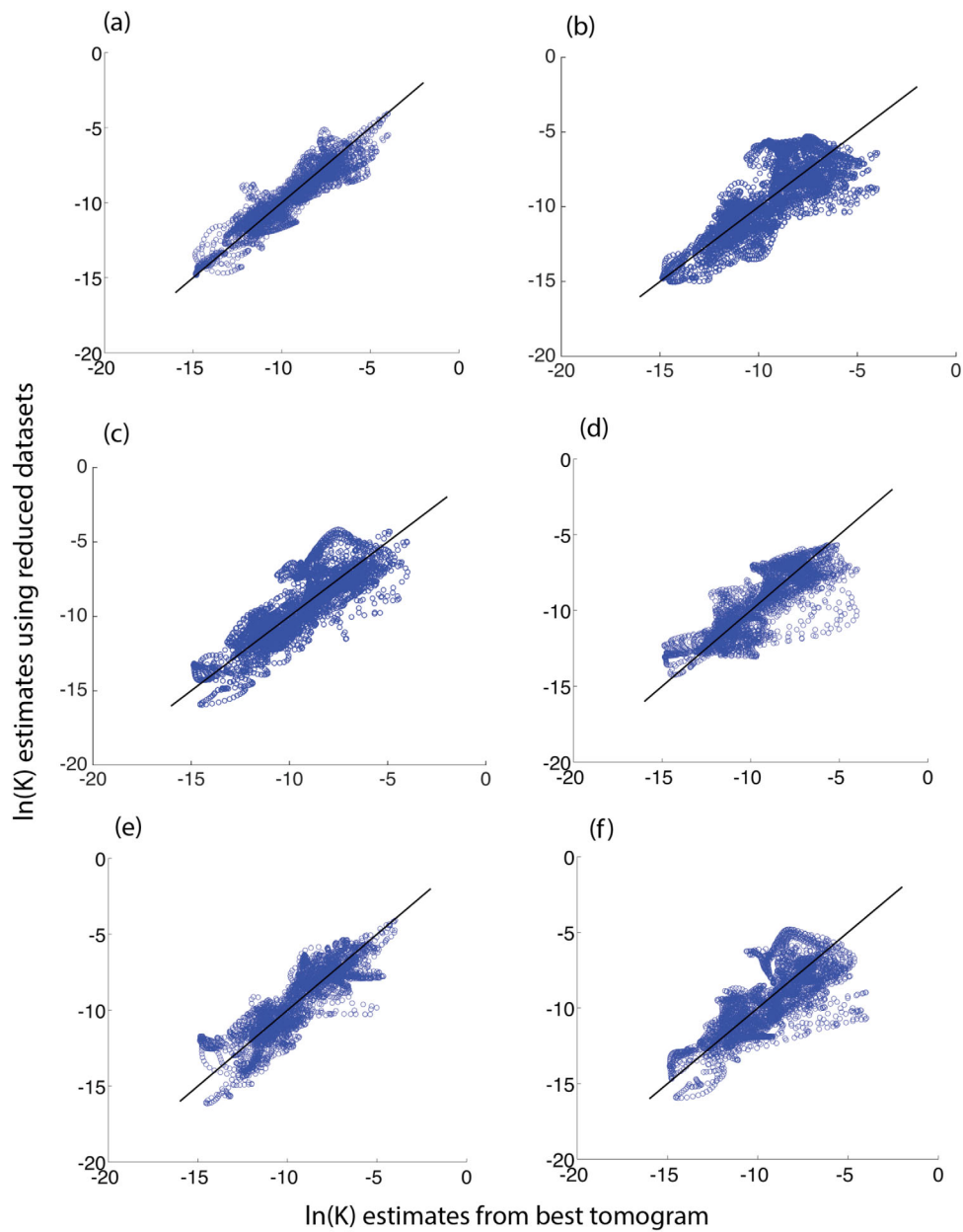


Figure 12. Scatterplot comparing K tomogram from reduced data sets against best tomogram result. Each subplot corresponds with associated tomogram in Figure 11.

The K tomogram incorporating five sources provides an even more detailed characterization of the heterogeneous features. This is also true when we look at the S_s tomogram, with more detailed S_s features becoming apparent as more pumping tests are inverted. We also notice that the K tomograms are not significantly correlated with S_s tomograms. This is likely due to the fact that S_s is fairly consistent across different types of aquifer materials, as discussed in Yin and Illman [2009]. We also note, qualitatively, that improvement in imaging with multiple pumping tests is comparable to improvement of using multiple testing frequencies for a single pumping test (e.g., Figure 9d versus Figure 10c).

6.3. Receiver Location Influence on K Tomogram

In this section, we looked into receiver locations' influence on K tomograms while keeping the number of source locations constant (three pumping tests). We designated receivers as three separate concentric arrays, with the inner array indicated by white solid points on Figure 11b, middle array as white solid points

Table 1. Results From All Inversions Performed^a

Analysis Case	Test Periods Included (s)	Pumping Locations Included	Observation Locations Included	Avg. $\ln(K)$ (\ln (m/s))	$\sigma^2_{\ln K}$	Data RMSE	Model RMSE
1	2	c3r3	1–11	−10.68	2.32	2.95E-03	1.54
2	5	c3r3	1–11	−10.64	1.50	2.07E-03	1.57
3	10	c3r3	1–11	−11.02	2.48	3.40E-03	2.15
4	20	c3r3	1–11	−11.48	2.88	4.98E-03	1.96
5	2, 5	c3r3	1–11	−11.48	4.23	8.67E-03	2.08
6	2, 10	c3r3	1–11	−11.31	3.52	4.33E-03	1.76
7	2, 20	c3r3	1–11	−12.17	5.36	1.50E-02	2.57
8	5, 10	c3r3	1–11	−10.93	1.86	2.01E-03	1.65
9	10, 20	c3r3	1–11	−11.00	1.80	2.37E-03	1.70
10	2, 5, 10	c3r3	1–11	−11.32	3.57	3.45E-03	1.71
11	2, 5, 20	c3r3	1–11	−11.78	4.39	4.93E-03	2.26
12	5, 10, 20	c3r3	1–11	−10.96	1.97	1.64E-03	1.69
13	2, 5, 10, 20	c3r3	1–11	−10.93	3.79	5.07E-03	1.53
14	2	c1r2, c2r4, c3r3, c4r1, c5r5	1–11	−10.29	1.91	1.11E-03	1.56
15	5	c1r2, c2r4, c3r3, c4r1, c5r5	1–11	−10.58	1.95	9.31E-04	1.42
16	10	c1r2, c2r4, c3r3, c4r1, c5r5	1–11	−10.79	1.90	1.13E-03	1.31
17	20	c1r2, c2r4, c3r3, c4r1, c5r5	1–11	−11.41	2.94	2.58E-03	1.58
18	2, 5, 10, 20	c1r2	1–11	−11.84	2.84	5.01E-03	1.78
19	2, 5, 10, 20	c1r2, c2r4	1–11	−11.34	2.88	3.52E-03	1.58
20	2, 5, 10, 20	c1r2, c2r4, c3r3	1–11	−11.44	3.46	2.09E-03	2.08
21	2, 5, 10, 20	c1r2, c2r4, c3r3, c4r1	1–11	−10.92	3.61	4.93E-04	1.28
22	2, 5, 10, 20	c1r2, c2r4, c3r3, c4r1, c5r5	1–11	−10.91	4.38	4.52E-04	0.00
23	2, 5, 10, 20	c1r2, c3r3, c5r5	5–11	−11.17	3.18	2.99E-03	1.70
24	2, 5, 10, 20	c1r2, c3r3, c5r5	1–4, 6, 8, 10, 11	−10.96	2.95	1.48E-03	1.54
25	2, 5, 10, 20	c1r2, c3r3, c5r5	1–4, 5, 7, 9	−11.29	3.83	1.17E-03	1.94
26	2, 5, 10, 20	c1r2, c3r3, c5r5	1, 2, 3, 4	−10.86	1.89	2.23E-03	1.53
27	2, 5, 10, 20	c1r2, c3r3, c5r5	5, 7, 9	−11.23	2.70	4.99E-03	1.84
28	2, 5, 10, 20	c1r2, c3r3, c5r5	6, 8, 10, 11	−11.07	1.73	1.80E-03	1.81

^aAnalysis cases vary according to pumping periods inverted (column 2), pumping locations included (column 3), and observations included (column 4, see Figure 3). Tomogram results are quantified in terms of their mean $\ln(K)$ values, $\ln(K)$ variance, data RMSE, and model RMSE. Data RMSE refers to root-mean-squared error for tomogram when fitting all data. Model RMSE quantifies difference between obtained tomogram and case 22, in which all data were inverted.

on Figure 11d, and outer array as white solid points on Figure 11f. We assume that the receiver data from these white points are available in each corresponding tomogram. It is notable that when using only the inner or the middle array of receiver data, we can also obtain a K tomogram that clearly represents the sandbox K pattern (see Figures 11b and 11d). When using only the outer array of receiver data, the K tomogram does not provide as clear of a description of aquifer heterogeneity. This is likely due to the fact that the distance between source and outer array of receivers is further; therefore, the transmitted signal dissipates more and contains less information for aquifer characterization. A direct comparison between K tomograms with varied receivers (Figure 11) and the best K tomogram (Figure 8b) is also presented in Figure 12.

6.4. Quantification of K Tomogram Trends and Variability

We next compare the results of OHT across a range of analysis cases in order to quantitatively assess overall trends. To do this, we compute for each tomogram the geometric mean of log scale K ($\ln K$), the variance of $\ln K$, data root-mean-squared errors (RMSE), and model RMSE. Data RMSE is defined here as the RMSE obtained when the given tomogram is utilized to simulate *all* collected data (i.e., data collected across all pumping tests, observation locations, and frequencies). Assuming that our inversion of all data (Case 22) is closest to the true sandbox parameter values, we calculate the model RMSE defined as the difference between the given analysis case's parameter estimates and those obtained from analysis Case 22. Note that the actual K distribution in the sandbox is affected by packing and other experimental issues. It is for this reason that we employ comparison between the best K tomogram (Case 22) and others, rather than assuming that the visible heterogeneity in the sandbox can be treated as a "known" distribution.

In Table 1, we find that the mean $\ln(K)$ computed from various K tomograms is relatively lower than the $\ln(K)$ values obtained from permeameter measurements of either porous media material. Initially, it was suspected that this could have resulted from compaction of the porous media inside the sandbox. However, analysis of simple drawdown data collected during a constant-rate pumping test—in which water was

extracted from the confined constant head aquifer at a rate of $5\text{cm}^3/\text{s}$ —resulted in an estimated $\ln(K)$ value of -9.1 , contradicting this idea.

Previously, we have shown that when using one pumping location (column 3 row 3, i.e., c3r3 in Table 1), gradually including data from additional pumping periods appears to visually improve the K tomogram (Figure 9), although statistical comparison on Table 1, rows 1–13, is not in complete agreement with this visual comparison. K tomograms using single frequency from all five pumping tests generally have low misfit in terms of both data RMSE and model RMSE (Table 1, rows 14–17), suggesting that the use of multiple pumping locations is still clearly beneficial for OHT. Similarly, considering the cases where all the pumping frequencies are used in inversion (Table 1, rows 18–22), the K tomogram errors are reduced with increasing numbers of pumping test locations. When using only partial observation locations' data in multifrequency inversion (Table 1, rows 23–28), model and data misfit are surprisingly small, suggesting that multifrequency data can to some extent make up for low observational density.

7. Conclusions and Future Work

This is the first comprehensive evaluation of Oscillatory Hydraulic Tomography applied to a real (laboratory scale) aquifer. To process and invert the collected data efficiently, we convert the groundwater flow equation to a phasor domain [see *Cardiff et al.*, 2013] and represent the oscillatory head data using Fourier coefficients. Data collected from the sandbox were likewise processed using the Fast Fourier Transform in order to obtain the dominant signal components. This approach allows estimation of both heterogeneous conductivity and storage coefficients—with drastically improved modeling efficiency, if compared to a fully transient hydraulic tomography analysis—and obtains comparable imaging results to earlier sandbox experiments using traditional hydraulic tomography approaches.

Visualization of all developed tomograms showed that in almost all cases, OHT was able to detect major heterogeneous features within the sandbox. While results from quantitative metrics such as RMSE are somewhat mixed, multifrequency joint inversion appears to be able to improve K tomograms when compared to a single frequency inversion. However, as in traditional hydraulic tomography, improved availability of pumping test data from multiple locations appears to offer the most improvement. Based on these laboratory experimental results, we have developed the following insights which should be useful for field applications of OHT:

1. For single source and multireceiver OHT, locating the source at the center of the receiver array will help to obtain the best characterization of the K field;
2. When the number of pumping and/or measurement locations is limited, more resolved images of heterogeneity can be obtained by performing OHT at a range of frequencies. OHT thus may provide an excellent method for improving characterization results when the number of wells available at a field site is limited;
3. That said, including multiple pumping tests at different locations within the aquifer is highly beneficial, especially for reducing predictive errors (data RMSE).

We believe that the data collected via OHT, if applied in the field, are more reliable than constant-rate pumping test data, which are often affected by noises and more difficult to separate from other background signals that may occur during pumping tests (e.g., evapotranspiration and other nearby pumping wells). It is also a promising technique for characterizing contaminated sites, in that OHT minimally impacts groundwater flow fields during the process of testing. Based on qualitative comparisons with earlier sandbox tomography data sets, OHT appears to provide comparable imaging results to existing HT technologies. However, the unique aspects of OHT allow improved data signal-to-noise ratios, reduced data collection time, and (most especially) drastically increased analysis efficiency thanks to fast numerical modeling.

In future work, we would like to perform more detailed comparisons between OHT and other suggested hydraulic tomography characterization strategies, including transient hydraulic tomography (THT) inversion of data from constant-rate pumping tests, and travel time/amplitude inversion of data from slug testing [e.g., *Brauchler et al.*, 2007]. Additional investigation is also necessary to determine why our inversions exhibit poor convergence if the theoretically correct data error magnitudes (following *Bakhos et al.* [2014]) are used for inverting multifrequency data. A best practice for future investigations may be to utilize

restricted maximum likelihood techniques [Kitanidis, 1995] to automatically determine data weights at different periods, a method which can be investigated using the dataset presented here. Finally, analysis of application of OHT at the field scale has not yet been carried out—further investigations of theoretical and logistical issues present in field-scale aquifer characterization will be an area of continuing interest for future work.

Acknowledgments

This work was funded by NSF grant EAR-1215746, "Collaborative Research: Fundamental Research on Oscillatory Flow in Hydrogeology" and by Weeks RA research assistantship at University of Wisconsin-Madison. Raw time series data from the sandbox experiments are available upon request from the corresponding author. We would like to thank the insightful and detailed comments of Todd Rasmussen and two anonymous reviewers, whose efforts greatly contributed to this manuscript. In addition, we would like to thank Brian Berkowitz for his advice in design and operation of the laboratory sandbox.

References

- Bakhos, T., M. Cardiff, W. Barrash, and P. K. Kitanidis (2014), Data processing for oscillatory pumping tests, *J. Hydrol.*, 511, 310–319.
- Becker, M., and E. Guiltinan (2010), Cross-hole periodic hydraulic testing of inter-well connectivity, in *Stanford Geothermal Workshop*, SGP-TR-188, Stanford Univ., Stanford, Calif.
- Berg, S., and W. Illman (2011), Three-dimensional transient hydraulic tomography in a highly heterogeneous glaciofluvial aquifer-aquitard system, *Water Resour. Res.*, 47, W10507, doi:10.1029/2011WR010616.
- Berg, S., and W. Illman (2013), Field study of subsurface heterogeneity with steady-state hydraulic tomography, *Ground Water*, 51(1), 29–40, doi:10.1111/j.1745-6584.2012.00914.x.
- Bernabe, Y., U. Mok, and B. Evans (2005), A note on the oscillating flow method for measuring rock permeability, *Int. J. Rock Mech. Min. Sci.*, 43, 311–316.
- Black, J. H., and K. L. Kipp (1981), Determination of hydrogeological parameters using sinusoidal pressure tests: A theoretical appraisal, *Water Resour. Res.*, 17(3), 686–692.
- Brauchler, R., R. Liedl, and P. Dietrich (2003), A travel time based hydraulic tomographic approach, *Water Resources Res.*, 39(12), 1370, doi:10.1029/2003WR002262.
- Brauchler, R., J.-T. Cheng, P. Dietrich, M. Everett, B. Johnson, R. Liedl, and M. Sauter (2007), An inversion strategy for hydraulic tomography: Coupling travel time and amplitude inversion, *J. Hydrol.*, 345, 184–198.
- Butler, J. J., Jr., and W. Z. Liu (1993), Pumping tests in nonuniform aquifers: The radially asymmetric case, *Water Resour. Res.*, 29(2), 259–269.
- Cardiff, M., and W. Barrash (2011), 3-D transient hydraulic tomography in unconfined aquifers with fast drainage response, *Water Resour. Res.*, 47, W12518, doi:10.1029/2010WR010367.
- Cardiff, M., W. Barrash, and P. K. Kitanidis (2012), A field proof-of-concept of aquifer imaging using 3-D transient hydraulic tomography with modular, temporarily emplaced equipment, *Water Resour. Res.*, 48, W05531, doi:10.1029/2011WR011704.
- Cardiff, M., T. Bakhos, P. K. Kitanidis, and W. Barrash (2013), Aquifer heterogeneity characterization with oscillatory pumping: Sensitivity analysis and imaging potential, *Water Resour. Res.*, 49, 5395–5410, doi:10.1002/wrcr.20356.
- Guiltinan, E., and M. W. Becker (2015), Measuring well hydraulic connectivity in fractured bedrock using periodic slug tests, *J. Hydrol.*, 521, 100–107.
- Illman, W., A. Craig, and X. Liu (2008), Practical issues in imaging hydraulic conductivity through hydraulic tomography, *Ground Water*, 46(1), 120–132, doi:10.1111/j.1745-6584.2007.00374.x.
- Illman, W., S. J. Berg, X. Liu, and A. Massi (2010a), Hydraulic/partitioning tracer tomography for DNAPL source zone characterization: Small-scale sandbox experiments, *Environ. Sci. Technol.*, 44(22), 8609–8614.
- Illman, W., J. Zhu, A. J. Craig, and D. Yin (2010b), Comparison of aquifer characterization approaches through steady state groundwater model validation: A controlled laboratory sandbox study, *Water Resour. Res.*, 46, W04502, doi:10.1029/2009WR007745.
- Illman, W. A., S. J. Berg, and Z. Zhao (2015), Should hydraulic tomography data be interpreted using geostatistical inverse modeling? A laboratory sandbox investigation, *Water Resour. Res.*, 51, 3219–3237, doi:10.1002/2014WR016552.
- Kitanidis, P. K. (1995), Quasi-linear geostatistical theory for inversing, *Water Resour. Res.*, 31(10), 2411–2419.
- Koltermann, C. E., and S. M. Gorelick (1996), Heterogeneity in sedimentary deposits: A review of structure-imitating, process-imitating, and descriptive approaches, *Water Resour. Res.*, 32(9), 2617–2658, doi:10.1029/96WR00025.
- Kuo, C. H. (1972), Determination of reservoir properties from sinusoidal and multirate flow tests in one or more wells, *Soc. Pet. Eng. J.*, 12, 499–506.
- Lavenue, M., and G. de Marsily (2001), Three-dimensional interference test interpretation in a fractured aquifer using the Pilot Point Inverse Method, *Water Resour. Res.*, 37(11), 2659–2675, doi:10.1029/2000WR000289.
- Li, W., W. Nowak, and O. A. Cirpka (2005), Geostatistical inverse modeling of transient pumping tests using temporal moments of drawdown, *Water Resour. Res.*, 41(W08403), 1–13.
- Liu, S., J. T.-C. Yeh, and R. Gardiner (2002), Effectiveness of hydraulic tomography: Sandbox experiments, *Water Resour. Res.*, 38(4), 1034, doi:10.1029/2001WR000338.
- Liu, X., and P. K. Kitanidis (2011), Large-scale inverse modeling with an application in hydraulic tomography, *Water Resour. Res.*, 47, W02501, doi:10.1029/2010WR009144.
- Liu, X., W. Illman, A. Craig, J. Zhu, and T.-C. J. Yeh (2007), Laboratory sandbox validation of transient hydraulic tomography, *Water Resour. Res.*, 43, W05404, doi:10.1029/2006WR005144.
- Maineult, A., E. Strobach, and J. Renner (2008), Self-potential signals induced by periodic pumping tests, *J. Geophys. Res.*, 113, B01203, doi:10.1029/2007JB005193.
- Rabinovich, A., W. Barrash, M. Cardiff, D. L. Hochstetler, T. Bakhos, G. Dagan, and P. K. Kitanidis (2015), Frequency dependent hydraulic properties estimated from oscillatory pumping tests in an unconfined aquifer, *J. Hydrol.*, 531, 2–16, doi:10.1016/j.jhydrol.2015.08.021.
- Rasmussen, T. C., K. G. Haborak, and M. H. Young (2003), Estimating aquifer hydraulic properties using sinusoidal pumping at the Savannah River site, South Carolina, USA, *Hydrogeol. J.*, 11(4), 466–482.
- Renner, J., and M. Messar (2006), Periodic pumping tests, *Geophys. J. Int.*, 167(1), 479–493.
- Vargas-Guzman, A. J., and T.-C. J. Yeh (2002), The successive linear estimator: A revisit, *Adv. Water Resour.*, 25, 773–781.
- Vasco, D. W., H. Keers, and K. Karasaki (2000), Estimation of reservoir properties using transient pressure data: An asymptotic approach, *Water Resour. Res.*, 36(12), 3447–3465.
- Yeh, J. T.-C., and S. Liu (2000), Hydraulic tomography: Development of a new aquifer test method, *Water Resour. Res.*, 36(8), 2095–2105.
- Yin, D., and W. Illman (2009), Hydraulic tomography using temporal moments of drawdown recovery data: A laboratory sandbox study, *Water Resour. Res.*, 45, W01502, doi:10.1029/2007WR006623.
- Zhao, Z., W. A. Illman, T.-C. J. Yeh, S. J. Berg, and D. Mao (2015), Validation of hydraulic tomography in an unconfined aquifer: A controlled sandbox study, *Water Resour. Res.*, 51, 4137–4155, doi:10.1002/2015WR016910.

Aquifer imaging with pressure waves—Evaluation of low-impact characterization through sandbox experiments

Zhou, Yao Quan; David, Lim; Fausto, Cupola; Cardiff, Michael

- 01 Tanmoy Das Page 1
15/2/2019 17:37
- 02 Tanmoy Das Page 1
15/2/2019 6:38
- 03 Tanmoy Das Page 1
15/2/2019 17:36
- 04 Tanmoy Das Page 2
15/2/2019 7:49
- 05 Tanmoy Das Page 2
15/2/2019 7:50
- 06 Tanmoy Das Page 2
15/2/2019 7:52
- 07 Tanmoy Das Page 2
15/2/2019 7:56
- 08 Tanmoy Das Page 3
15/2/2019 7:57
- 09 Tanmoy Das Page 3
15/2/2019 7:58

10 Tanmoy Das

Page 3

15/2/2019 8:01

11 Tanmoy Das

Page 3

15/2/2019 8:02

12 Tanmoy Das

Page 6

20/5/2019 9:46

13 Tanmoy Das

Page 6

20/5/2019 9:46

14 Tanmoy Das

Page 7

16/10/2019 11:54

15 Tanmoy Das

Page 15

15/2/2019 6:45

16 Tanmoy Das

Page 15

15/2/2019 6:45

17 Tanmoy Das

Page 16

15/2/2019 6:45